

Volcanic ash forecast during the June 2011 Córdón Caulle eruption

Estela Collini · María Soledad Osores · Arnau Folch · José G. Viramonte · Gustavo Villarosa · Graciela Salmuni

Received: 18 November 2011 / Accepted: 6 November 2012 / Published online: 19 November 2012
© Springer Science+Business Media Dordrecht 2012

Abstract We modelled the transport and deposition of ash from the June 2011 eruption from Córdón Caulle volcanic complex, Chile. The modelling strategy, currently under development at the Argentinean Naval Hydrographic Service and National Meteorological Service, couples the weather research and forecasting (WRF/ARW) meteorological model with the FALL3D ash dispersal model. The strategy uses volcanological inputs inferred from satellite imagery, eruption reports and preliminary grain-size data obtained during the first days of the eruption from an Argentinean ash sample collection network. In this sense, the results shown here can be regarded as a quasi-syn-eruptive forecast for the first 16 days of the eruption. Although this article describes the modelling process in the aftermath of the crisis, the strategy was implemented from the beginning of the eruption, and results were made available to the Buenos Aires Volcanic Ash Advisory Centers and other end users. The model predicts ash cloud trajectories, concentration of ash at relevant flight levels, expected deposit thickness and ash accumulation rates at relevant localities. Here, we validate the modelling strategy by comparing results with satellite retrievals and syn-eruptive ground deposit measurements. Results highlight the goodness of the combined WRF/ARW-FALL3D forecasting system and point out the usefulness of coupling both models for short-term forecast of volcanic ash clouds.

E. Collini (✉) · M. S. Osores
Servicio de Hidrografía Naval (SHN) and Servicio Meteorológico Nacional (SMN), Buenos Aires,
Argentina
e-mail: estela.collini@gmail.com; eacollini@hidro.gov.ar

A. Folch
CASE Department, Barcelona Supercomputing Center-Centro Nacional de Supercomputación
(BSC-CNS), Barcelona, Spain

J. G. Viramonte
INENCO-GEONORTE (UNSa-CONICET), Salta, Argentina

G. Villarosa
INIBIOMA, CRUB (CONICET-Universidad Nacional del Comahue), Bariloche, Argentina

G. Salmuni
CONAE, Buenos Aires, Argentina

Keywords Cordon Caulle volcanic complex · Meteorological model · Ash cloud forecast · FALL3D model

1 Introduction

After decades of quiescence, the Puyehue-Cordón Caulle volcanic complex (PCCVC; Chile) erupted on Saturday 4 June 2011 from a new vent located 7 km NNW from the Puyehue stratovolcano (40.5°S, 72.2°W, 2,236 m a.s.l.). The initial explosive phase of the eruption, spanning for more than two weeks, was characterised by eruption columns oscillating between 7 and 12 km in height (a.s.l.). As it typically occurs in midlatitude Central and South Andean eruptions (e.g. Folch et al. 2008), the dominant regional winds directed the ash clouds over the Andes and caused abundant ash fallout across the Argentinean provinces of Río Negro, Neuquén and Chubut (in part, of course, also affecting the proximal areas in Chile). As occurred in 2008 during the Chaitén eruption, ash fallout impacted on agriculture, livestock, water distribution systems and ground and air transportation networks, affecting heavily the farming and tourism sectors of the Argentinean Patagonia. On the other hand, the finest granulometric fraction of the ash clouds and the accompanying volcanic aerosols circumvented the Southern Hemisphere passing over South Africa, South of Australia and New Zealand to reach again Chile after about 10 days. The presence of airborne ash caused major air traffic disruption in Argentina and, to a lesser extent, across the Southern Hemisphere towards Australia and New Zealand. Although less disruptive than the 2010 Eyjafjallajökull eruption in Iceland, the Cordón Caulle eruption stranded thousands of passengers worldwide due to cancellation of flights and caused also enormous economic loss to airlines. This eruption evidenced again the global nature of the volcanic ash dispersion phenomena and remarked the need for establishing efficient transnational coordination actions to manage volcanic crisis.

An important consequence of the 2010 Eyjafjallajökull eruption in Iceland was the introduction of quantitative criteria based on ash concentration thresholds to decide which airspace to close. Thus, new guidelines were adopted in Europe to discern zones of moderate (ash concentration between 0.2 and 2 mg/m³) and high (ash concentration above 2 mg/m³) contamination. At present, it is still unclear whether these or similar concentration thresholds will become regulatory, but several Volcanic Ash Advisory Centers (VAACs) and other institutions working at operational level do already issue quantitative forecasts to complement the still official “zero ash tolerance” products. In this context, crucial aspects to improve the accuracy of forecasts are to better quantify the source term (i.e. to estimate ash mass emission rate, eruption column height, vertical distribution of mass in the eruption column, and particle total grain-size distribution), to combine models and observations through data assimilation and to validate the modelling strategies. The recent eruptions of Eyjafjallajökull (Iceland, April–May 2010), Grímsvötn (Iceland, May 2011) and Cordón Caulle (Chile, June–July 2011) provide excellent case studies to the last purpose.

Here, we model the transport and deposition of ash during the main explosive phase of the 2011 Cordón Caulle eruption using the WRF/ARW-FALL3D modelling system as if in operational mode. Meteorological inputs are furnished by concatenating short-term (72 h) WRF/ARW forecasts. Volcanological inputs are obtained from different eruption reports and observations available at the time of the eruption, including preliminary grain-size analysis of samples collected at key locations. Our final goal is to validate the operational modelling strategy still under development by the Argentinean Naval Hydrographic Service

(SHN) in collaboration with the National Meteorological Service (SMN), INENCO (Instituto de Energía no Convencional)-GEONORTE, UNSa-CONICET, INIBIOMA (Instituto de Investigaciones en Biodiversidad y Medioambiente), Universidad Nacional del Comahue-CONICET and the Barcelona Supercomputing Center (BSC-CNS) in the frame of the international network CENIZA (www.bsc.es/case/projects/ceniza/). For this, we compare the simulations with satellite retrievals and measurements of deposit thickness. In this sense, this work complements previous validations of the modelling strategy already done for the Chaitén 2008 (Folch et al. 2008; Folch et al. 2011) and the Hudson 1991 eruptions (Osores et al. 2011).

The manuscript is arranged as follows. Firstly, we present an overview of the geological setting of the PCCVC (Sect. 2) and a brief chronology of the 2011 eruption (Sect. 3) in which we emphasise those aspects that are relevant to our purpose of model validation. Secondly, we explain the early sampling strategy and present a preliminary chemical and petrographic analysis of the ash samples (Sect. 4). Thirdly, we summarise the current WRF/ARW-FALL3D modelling strategy at SMN, including the configuration of the meteorological driver (WRF/ARW) and the ash transport (FALL3D) model and the selection of volcanological inputs (Sect. 5). Finally, we present the results, validate the modelling strategy (Sect. 6), and conclude with a discussion on the implications for operational forecasts (Sect. 7).

2 Geological setting of the PCCVC

The PCCVC (Fig. 1a) is a cluster of Pleistocene to recent volcanic vents aligned along a NW–SE trend oblique to the main volcanic front of the Southern Andes Volcanic Zone (SVZ). The volcanic front runs parallel to the Chile-Peru trench that, at this latitude, trends sub-meridional (79°E) with a rate of plate convergence of around 7.9 cm/year (DeMets et al. 1994; Tamaki 2000). The volcanic arc is 60–70 km wide, the Wadatti-Benioff zone dips 30°, and the crust thickness is about 38–40 km (Hildreth and Moorbath 1988; Cahill and Isacks 1992; Tassara and Yáñez 2003). The PCCVC consists of a transversal 15 km long by 4 km wide ridge oriented in a NW–SE direction (135° of azimuth) that includes a nested graben and a cluster of fissure vents with aligned domes and pyroclastic cones (Moreno 1977; Lara et al. 2004, 2006a, b; Lara and Moreno 2006; Singer et al. 2008). The eruptive centres extend between the Pleistocene Cordillera Nevada caldera (1,799 m a.s.l.), located at the NW of the PCCVC, and the Puyehue stratovolcano, located at the SE (Campos et al. 1998; Lara et al. 2001, 2003).

From a structural point of view, the PCCVC rests upon the trace of the Liquiñe–Ofqui fault, a ca. 1,000 km long first order intra-arc structure related to a dextral transpressive regime active during the Quaternary times (Cembrano et al. 1996; Lavenu and Cembrano 1999) and to the pre Mesozoic Andean cycle NW–SE structures. Different authors (Lowell et al. 1995; Bentley 1997; Denton et al. 1999; Lara et al. 2006b) have pointed out the close spatial relationship between the crustal structure and volcanic centres of the PCCVC, especially during the last 14 ka. The PCCVC contains abundant basaltic and silicic lavas, domes, pyroclastic flow and fall deposits. Basaltic lavas were mainly erupted during the early stages and along the entire PCCVC, products of intermediate compositions dominate in the Puyehue stratovolcano, and the most silica-rich magmas were erupted mainly as domes and fissural eruptions throughout the Cordón Caulle volcanic complex fissure system (CCVC). Their chemical composition is mainly rhyodacitic to rhyolitic (68–71 % SiO₂; Gerlach et al. 1988 and Singer et al. 2008) with subordinated basaltic to

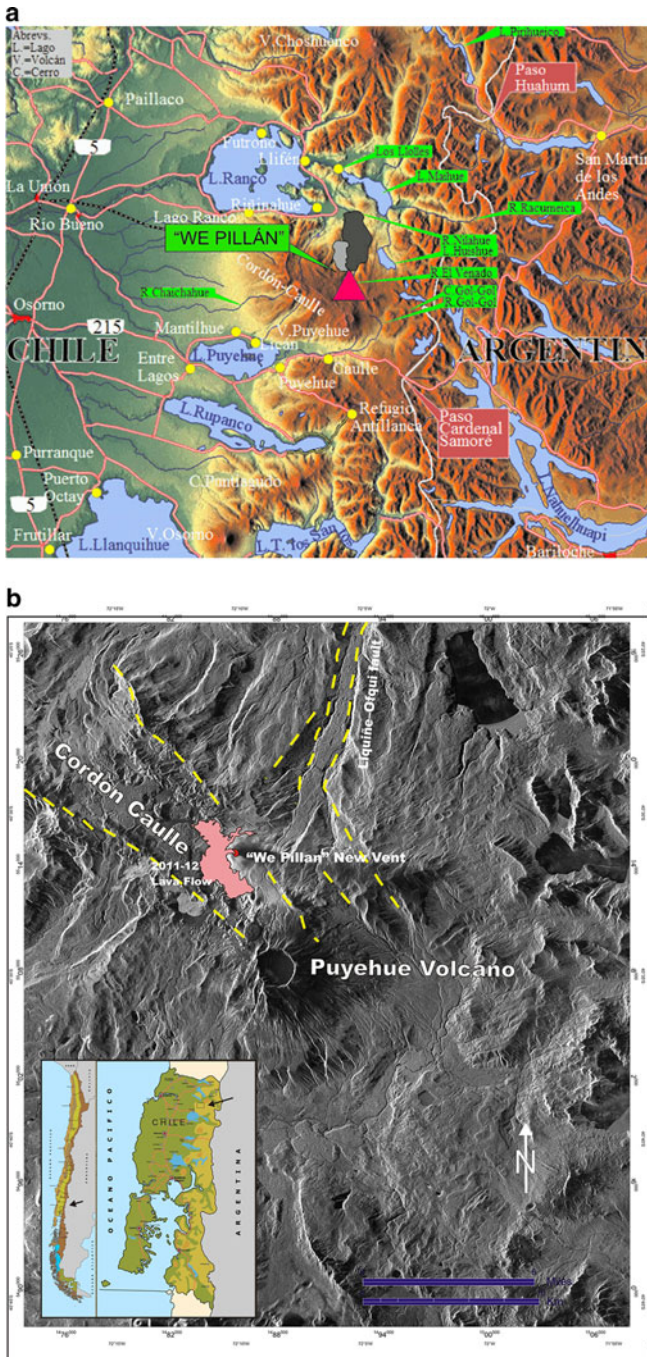


Fig. 1 **a** Location general map of the PCCVC. **b** Sketch map of the PCCVC showing the main morphologic features of the complex. **c** Detail of the location of the “We Pillán” new vent and its 2011–2012 lava flow. The COSMO-SkyMed Images, taken by the Italo-Argentinean Satellite system for development and emergency (SIASGE-ASI-CONAE), were used to build up the sketch map

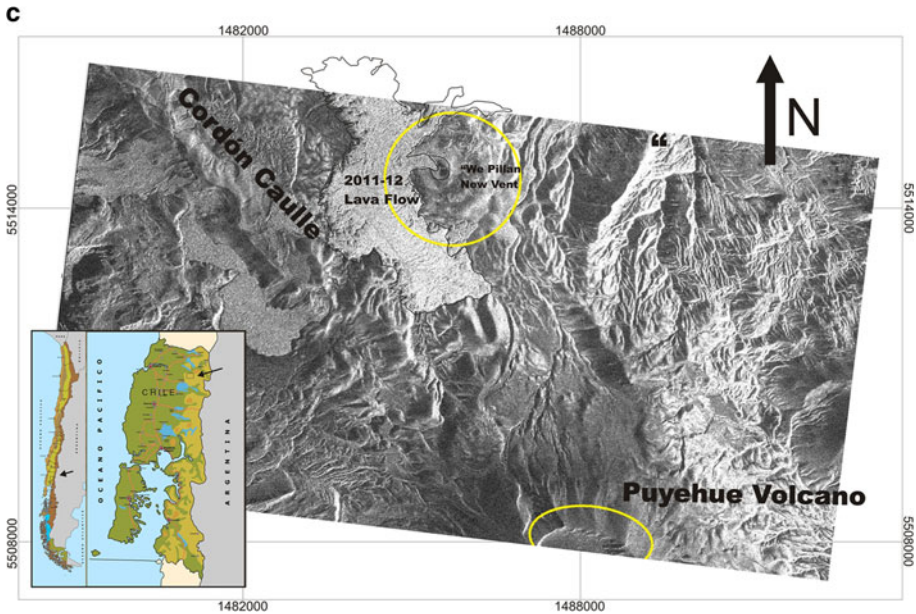


Fig. 1 continued

andesitic types. Such evolved compositions are uncommon in the SAVZ in general and, in particular, within the southern complexes of the SAVZ located between 37°S and 46°S of latitude, which typically present compositions ranging from basaltic to basaltic-andesitic.

According to Lara et al. (2004, 2006a), two major fissure eruptions, mainly rhyodacitic in composition (e.g. Moreno and Petit-Breuilh 1999), have occurred during the 20th century (1921–1922 and 1960), the latter only 38 h after the famous Valdivia 9.5 Mw earthquake (Kanamori and Cipar 1974). This was the largest earthquake instrumentally recorded and had the epicentre 240 km NW of the CCVC. It is worth noting that June 2011 eruption also occurred months after the last Chilean large earthquake (8.8 Mw; 27 February 2010), which had the epicentre in the Chilean sea (near Curanipe and Cobquecura), 475 km NW of the PCCVC. In addition to these major events, other minor fissure eruptions (VEI = 1–2) occurred in 1990, 1934, 1929, 1919, 1914, 1905, 1893 and 1759 according to the Smithsonian Global Volcanism Programme.

3 Chronology of the June 2011 eruption

During the last days of May 2011, the Chilean “Servicio Nacional de Geología y Minería” (SERNAGEOMIN), the scientific agency in charge of the eruption warning according to the Chilean protocols issued the red volcanic alert after recording an anomalous seismic activity in the area (up to 230 earthquakes per hour with 12 events of $M_w > 4$ and 50 events of $M_w > 3$). Based on the SERNAGEOMIN information, the Chilean National Emergency Office (ONEMI) declared the red alert in terms of civil protection and emergency response coordination. The eruption started on 4 June at 14:45 LT (18:45 UTC) with the opening of a new vent and the development of a vigorous sustained eruption column (Figs. 2, 3) that

raised 10–12 km according to reports from SERNAGEOMIN, ONEMI and Buenos Aires VAAC. We refer to this new vent as “We Pillán” (meaning “new vent” in Mapuche language).

The “We Pillán” vent opened probably at the joint of a secondary lineament (167° of azimuth) with the northern Cordon Caulle principal graben fault system at a distance of about 7 km NNW from the crater rim of the Puyehue volcano. The exact location of the vent, according to new geo-referenced satellite COSMO-SKYMED images, is $-40^\circ 31' 21.14''$ S/ $-72^\circ 08' 50.23''$ W (See Fig. 1b, c). In contrast to what happened during

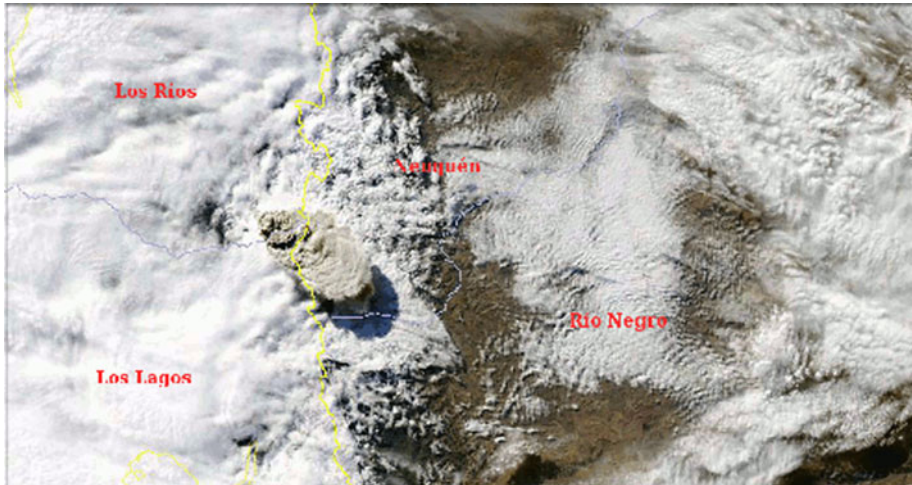


Fig. 2 MODIS Aqua image taken on 4 June at 18:50UTC and processed by the SMN. The image shows the initial development of the ash cloud. Cloud height was estimated between 10 and 12 km a.s.l



Fig. 3 Eruption column and ash cloud as seen from near Osorno city (Chile) on 5 June 2011 (Reuters/Air Force of Chile/Handout)

the previous 1921–1922 and 1960 eruptions, the 2011 eruption occurred only from a single vent. However, these three major historical events have several features in common: (1) the eruptive vents are associated to general NW–SE structures (135° of azimuth for 1921–1922 and 1960 eruptions, 167° for the 2011 event), (2) eruption of highly evolved magmas (dacitic in 1921–1922 and rhyodacitic in 1960 and 2011), (3) initial subplinian or plinian explosive phases with eruption column heights ranging between 7 and 12 km followed by more effusive phase and (4) eruptions lasting between 2 to several months. Here, we give a brief chronology of the events occurred during the first 2 months of activity (see the ONEMI website and the local press agencies for further details):

- On 27 April 2011, volcanologists from SERNAGEOMIN interpreted a seismic swarm located at 4 km depth as caused by magma movement in the volcanic system beneath CCVC.
- Along May 2011, seismic activity was persistent and of increasing intensity. Two major seismic events occurred on 4 and 17 May (Mw 3.5 and 4.2, respectively).
- On 1 June, SERNAGEOMIN reported dramatic changes in the volcano seismicity with many LP and HB events located SE from Cordón Caulle. Around 750 earthquakes were registered in only 32 h with hypocentres located at depths ranging between 2.5 and 5 km. The day after seismic activity increased to 25 earthquakes per hour and ONEMI changed the volcanic alert code for civil protection to yellow (level 3).
- Early on 3 June, seismicity (LP and HB events) increased to 60 earthquakes per hour with spasmodic tremors located at depths between 1 and 4 km. Later, up to 230–250 earthquakes per hour were registered, 12 of them with magnitude >4.5 Mw and 50 with magnitude >3.1 Mw. ONEMI changed the volcanic alert code to red (level 5), implying imminent volcanic eruption.
- On 4 June at 15:15 LT (19:15 UTC), ONEMI reported that the eruption had initiated at 14:45 LT (18:45 UTC), and a persistent plinian eruptive column 10–12 km high (a.s.l.) was already developed (Fig. 2).
- From 5–12 June, the column height fluctuated between 12 and 4 km (Fig. 3). The ash clouds reached the Atlantic coast during the 5 June early morning (LT) then turned NE to reach the N of Argentina during the 7 June and the city of Buenos Aires the days after. Flight operations were cancelled at the affected airports. In turn, the finest fraction of the clouds circumvented the Southern Hemisphere passing over the South of Australia on the 10 June and arriving again to South America during the 15 June. During this period, seismic events diminished progressively from 17 to 5 earthquakes per hour.
- From 13–15 June, fluctuating seismic tremors were detected in correspondence with sudden changes in the height of the eruptive column and suggesting instability in the magmatic system. From 16 June, tremors changed to low frequency harmonic tremors, and the eruption column height was around 3 km. This change suggested the ascent of a magmatic body.
- Finally, viscous lava was erupted on 20 June. Once the magma body reached the surface the harmonic tremors diminished to disappear on 23 June, when ONEMI changed the code to that of a minor eruption. The effusive phase is still ongoing on April 2012 (See Fig. 1b).

4 Sampling and features of the eruption products

4.1 Sampling of the fallout deposits

Collection of tephra samples and measurement of deposit thickness started in Bariloche on 4 June, minutes after the first ash fall (16:30 LT). Fall material was collected over regular

periods of time in which the evolution of the deposit thickness was also recorded. Tephra sampling and tephra thickness record in other affected areas started on 5 June, covering mainly proximal environments in the Nahuel Huapi National Park. All these samples are pristine and unaffected by hydrological or postdepositional aeolian processes. Data from medial and distal areas were collected from the 6 June and continued during the following months. However, we consider here preliminary data from the first 2 months of the eruption only.

The deposit from the first day at Puyehue, Villa La Angostura and Bariloche (located at distances <100 km from the vent) was remarkably coarse-grained, ranging from coarse lapilli to coarse ash. Ash collected eastwards and northwards becomes finer-grained as the deposit becomes thinner. Ash collection was carried out from (1) direct deposition in real time or immediately after deposition (undisturbed, pristine samples representing a single pulse) by one of the authors (G.V.) and colleagues, (2) deposited tephra collected few days after the fallout, (3) sample collection over a vast area during every ash fall event from a network that was set up during the first week of the eruption, operated with the assistance of park rangers from the Nahuel Huapi National Park, the border control force, and the

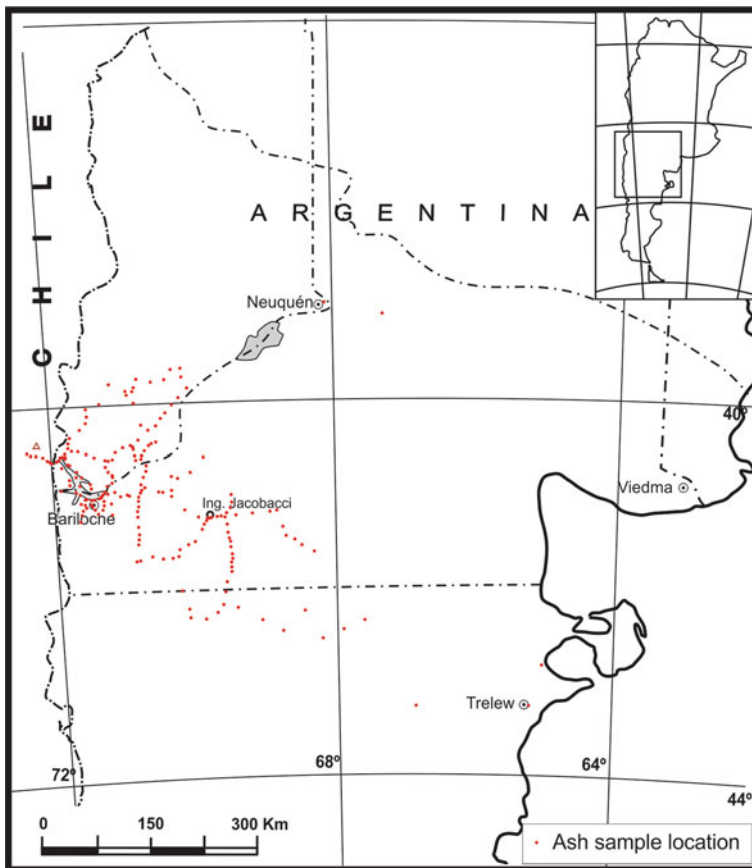


Fig. 4 Map showing the set of sample points where the collection of thickness measurements was carried out

municipal Civil Defence employees from the cities of Bariloche and Villa La Angostura. Most samples were collected at proximal and medial environments, within 250 km from the volcano. Distal samples were collected at Puerto Madryn, Neuquén, General Roca, Planta Las Lajas, and Comodoro Rivadavia (Fig. 4). Collection was carried out at around 400 sampling points, 199 of which were finally used (Fig. 4). Sampling followed a set of instructions for thickness measurements and conditions of collection adapted from IVHHN and USGS procedures (Villarosa and Outes 2008).

The most significant tephra were deposited mostly along a wide W–E elongated area between 40–42°S and up to 72°W. This area is characterised by a very strong precipitation gradient, ranging from 4,000 mm/year in the Andes, with a wet season during the winter, to <200 mm/year in the Patagonian steppe, where the scarce rainfall is distributed almost homogeneously throughout the year. This characteristic gradient defines diverse sedimentary environments that explain the significantly different depositional and postdepositional processes that occurred since the beginning of the eruption on 4 June. In mountainous environment (proximal areas), coarse-grained tephra is affected by rain and snow, and pyroclastic deposits suffer compaction and fluvial remobilization of fine ash and low-density pumice fractions, including lapilli and larger pumice fragments. This material was transported by rivers down to the lower basin, where thick floating deposits covered many rivers, lakes and even the distal portion of the Alicurá reservoir, more than 100 km away from the volcano. In contrast, in extra-Andean arid environments, the persistent strong winds affected tephra deposition and produced important resuspension and remobilization within hours after or even during the fallout events. Ground level remobilization of coarse ash and even fine lapilli (3–4 mm) during fallout was witnessed during sampling. Topography and vegetation played a strong control on depositional and postdepositional processes, being evident in many cases the presence of thickened deposits at wind protected areas and diminished thicknesses on plateaus and open flats exposed to strong winds (Fig. 5), even in the first week of the eruption. It is clear that vegetation played an important role as protected areas allowing the accumulation of tephra behind the shrubs, whereas erosion and formation of wind ripples were active processes in non-vegetated sectors. In this context, more than 300 thickness measurements were recorded during June and July 2011, and many of them were repeated at the same sites in order to control the evolution of tephra deposits. Thicknesses used for the isopach map were recorded paying special attention to avoid sites showing evidence of erosion, compaction or redeposition.

4.2 Chemical and petrographic analysis of the eruption products

Preliminary chemical and petrographic analysis of the sampled pyroclastic material was done in order to characterise the different materials released from the “We Pillán” vent. Proximal lapilli and coarse ash were used for this purpose. Microscopic studies revealed the presence of three principal types of juvenile pumice materials: white, brown and black glassy fragments, being white the most abundant (over 90 %) (Fig. 6). It was observed that all pumice fragments were strongly vesiculated (Fig. 6a). However, white pumices showed in many cases tubular vesiculation, while brown and black products had preferentially rounded vesicles (Fig. 6b, c). Generally, black pumices were less vesiculated.

Petrographic observation revealed in all pumices, the presence of scarce phenocryst of plagioclase (An₂₀), few little crystals of sanidine (observed by electronic microscope) and two types of pyroxenes (Ortho and Clyn pyroxenes), all of them immersed in a glassy matrix. Preliminary bulk XRF chemical major element analysis from the white pumice was



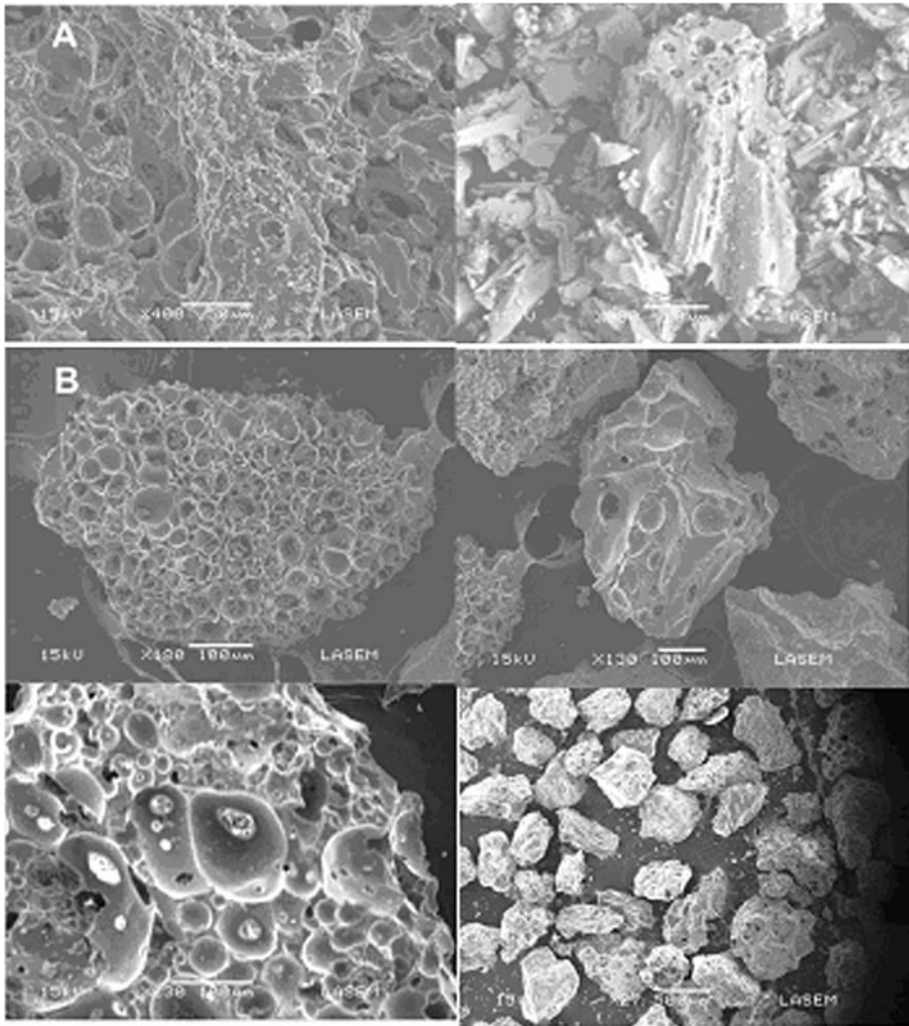
Fig. 5 Picture showing the intense remobilization during and immediately after deposition over the steppe (near Ingeniero Jacobacci, Argentina). Notice the accumulation of tephra behind the shrubs, as protected areas, erosion in non-vegetated sectors and wind ripples

carried out (Table 1) in order to identify its composition. The results are shown in Table 2 and characterised the pumice as Trachydacite-ryolite in the TAS Classification (Le Maitre et al. 2002), see Fig. 7. Preliminary discrete major element chemical analysis was carried out on glass using an EDS Electron Microscope. Results suggest the presence of at least two different juvenile “end members glasses:” basaltic-andesitic (55–60 % SiO_2 , lithics?) and rhyolitic (71–73 % SiO_2), whereas the intermediate compositions might represent a “hybrid” type, possibly from an incipient magma mixing processes (≈ 60 % SiO_2). These features are observed in previous eruptions from PCCVC (e.g. 1960 tephra), and in the 2.3 ka Nahuel Huapi Tephra (NHT), a thick rhyolitic white tephra that rapidly grades into a dark brown scoria (Villarosa et al. 2006; Chapron et al. 2006; Villarosa 2008), where similar juvenile pyroclastic components are present.

5 Modelling strategy

5.1 Meteorological modelling

The SHN–SMN runs a numerical weather prediction system composed by WPS, WRF/ARW (Michalakes et al. 2005), ARWpost and WPPV3 on a daily basis for the 00UTC cycle and using the GFS (NCEP) global model forecasts to furnish the initial field and boundary conditions to WRF/ARW. The SMN operational computational domain for WRF/ARW covers South America and the surrounding oceans with a spatial resolution of 24 km and provides 72 h of forecast with an output frequency of 3 h. The operational configuration includes the following physical parameterizations: (1) the Ferrier scheme (Eta), which is an accurate scheme for the microphysics using look-up tables for efficiency and accounts for multiple bands, trace gases and species, (2) the RRTM (rapid radiative transfer model) long wave radiative model (Mlawer et al. 1997), (3) the Dudhia scheme (Dudhia 1989) for shortwave radiation, which is a simple downwards integration allowing for efficient cloud and clear-sky absorption and scattering, (4) the Monin–Obukhov (Janjic-Eta) similarity scheme, based on similarity theory with viscous sub-layers both over



A: SEM White Pumice
B: SEM Black Pumice
C: SEM Brown Pumice

Fig. 6 SEM Images of three different types of juvenile pumice. **aLeft** close-up of a pyroclast surface which shows some coalescence of vesicles with varying vesicle-wall thickness in the centre of the image. **Right** Large tubular pyroclast showing septae or wall remnants of broken elongated vesicles. At the top of the fragment single vesicles with thick walls can also be seen. This pyroclast is surrounded by finer glass shards: blocky and Y shaped curved shards. **bLeft** Subrounded pumice pyroclast, highly vesiculated and thin vesicle walls with adhering dust. **Right** SEM of pumice pyroclast that shows low vesicularity with ovoid to slightly elongated vesicles separated by thick vesicle walls. Notice smooth fragmentation surfaces and evidence of vesicle coalescence at the top of the fragment. **cLeft** close-up of a highly vesiculated pyroclast, notice that there is evidence of coalescence of vesicles and presence of particles in vesicle hollows. **Right** SEM of vitric irregular to elongate pyroclasts, mostly pumiceous

Table 1 Preliminary discrete XRF bulk chemical major element analysis of the white pumice

Muestra N°	SiO ₂	Al ₂ O ₃	Fe ₂ O ₃	MnO	MgO	CaO	Na ₂ O	K ₂ O	P ₂ O ₅	TiO ₂	PPC	Total
Pu1406	69.57	14.20	4.06	0.11	0.87	2.06	5.60	2.71	0.12	0.68	0.5	100.47
Pu2206 3 “b”	69.33	14.02	3.82	0.11	0.86	1.97	5.48	2.77	0.13	0.66	1.02	100.17
Pu0806 7	69.38	13.85	3.58	0.11	0.81	2.03	5.42	2.67	0.11	0.62	0.930	99.51
Pu2206 3 “c”	69.12	14.01	3.98	0.11	0.86	2.01	5.53	2.71	0.11	0.66	1.10	100.20
Pu2206 3 “a”	69.20	14.08	3.95	0.10	0.85	1.95	5.38	2.72	0.12	0.63	1.05	100.04

Table 2 Preliminary discrete major element analysis of the Glass by EDS

% Oxides	WP	WP	BwP	BP
SiO ₂	71.74	66.34	60.45	55.70
Al ₂ O ₃	14.44	15.50	13.11	13.54
Fe ₂ O ₃	4.07	4.89	9.87	13.08
MgO		1.62	4.63	3.53
CaO	1.89	3.35	6.79	7.54
Na ₂ O	4.76	3.41	3.57	3.45
K ₂ O	3.11	3.76	1.58	1.26
TiO ₂	0.0	1.13	0.0	1.91
TOTAL	100.00	100.00	100.00	100.00

WP white pumice, *BwP* brown pumice, *BP* black pumice

solid surfaces and water points, (5) the Mellor-Yamada-Janjic (Eta) TKE scheme for the PBL and (6) the Betts-Miller-Janjic scheme for deep and shallow convection.

We used the WRF/ARW forecasts to obtain the necessary meteorological data during the simulated period, covering from 4 to 20 June 2011. Figure 8 gives different snapshots of the synoptic meteorological situation. At the beginning of the “We Pillán” vent eruption, during the 4 June, the sea level pressure pattern over Patagonia was dominated by a ridge extending from surface to high atmospheric levels. This high-pressure system generated weak to moderate NW surface winds over Patagonia (Fig. 8a). As this system moved northeast, a low-pressure system located over the Pacific Ocean, north of 45°S, displaced in the same direction and a second stronger low, located south of 45°S, displaced eastwards. On 6 June, at mid (~500 hPa) and high (~300 hPa) atmospheric levels, the wind over Patagonia rotated SW and became stronger, in association with the rare flank of the trough located north of 45°S. During the 7 June, this trough reached the northern limit of Paraguay, and the intense wind in the rare flank produced a strong SW advection of air from Patagonia (Fig. 8b). At the same time, the low-pressure system located south of 45°S generated a strong frontal zone over Patagonia that produced an extended cloudy zone covering the volcano until that afternoon. During this day and the following, fallout of snow and rain occurred over Patagonia. On the first hour of the 8 June, the wind at mid and high levels over the volcano region had a westerly component but, late in the afternoon, the direction rotated towards SW and the speed intensified in association with the rare flank of the trough. This situation is maintained until the 10

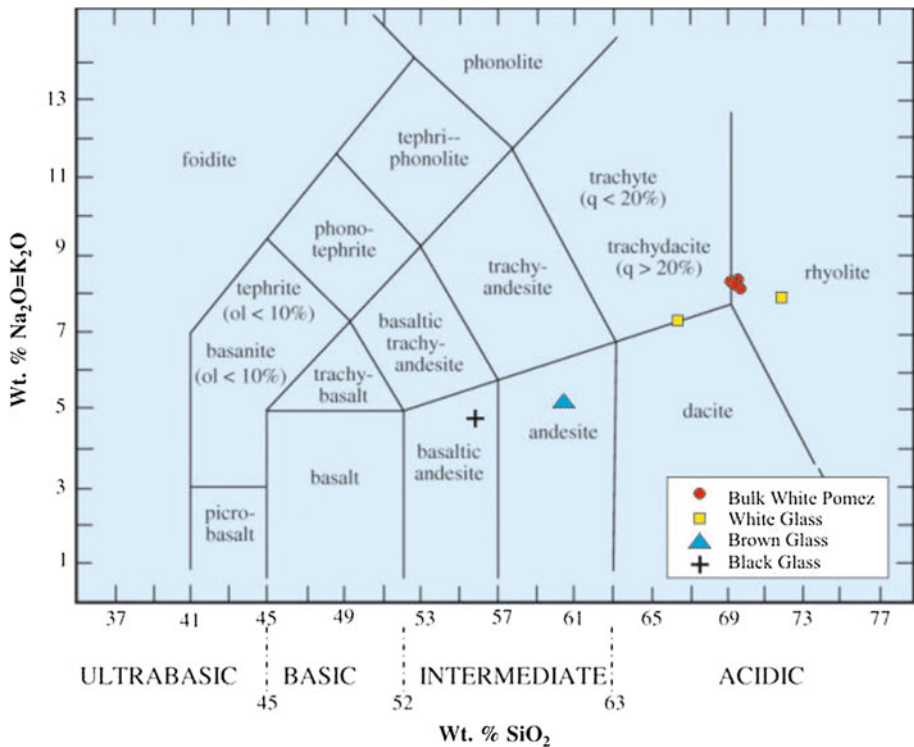


Fig. 7 Bulk major element XRF geochemistry of “We Pillán” white pumice and EDS punctual chemical analysis of different types of glasses (*White, brown and black*) using major element geochemistry TAS Classification (Le Maitre et al. 2002)

June (Fig. 8c, d). From 9 June to 11 June, a frontal zone passed through Patagonia, producing rain and snow fallout. On the 10 June, another trough advanced from the Pacific Ocean and the direction of the wind rotated towards west in all vertical levels. This low-pressure system generated a shallow trough that maintained the direction of wind unperturbed until 12 June. During this day, the front flank of a ridge penetrated over Patagonia from the west and, as a consequence of this intrusion, the wind rotated and maintained southwest until the 13 June (Fig. 8f), when the wind direction rotated again to the west because of the translation of the ridge. On the 14 June, the wind direction rotated northwest linked to the front flank of a low-pressure system located over the Pacific Ocean. As this system moved on, sustained NW winds developed over Patagonia (Fig. 8g). On 17 June, the north component of the wind intensified and the wind magnitude also increased. During this and the following days, a frontal zone affected the whole Patagonian region (Fig. 8h), and a dense cloud mass covered the area. Until the end of this study (20 June), the NW wind prevailed but with lower speed.

5.2 Volcanic ash transport and deposition modelling

We used the FALL3D dispersion model (Costa et al. 2006; Folch et al. 2009) to simulate the atmospheric dispersion and deposition of ash at ground. FALL3D uses 4D

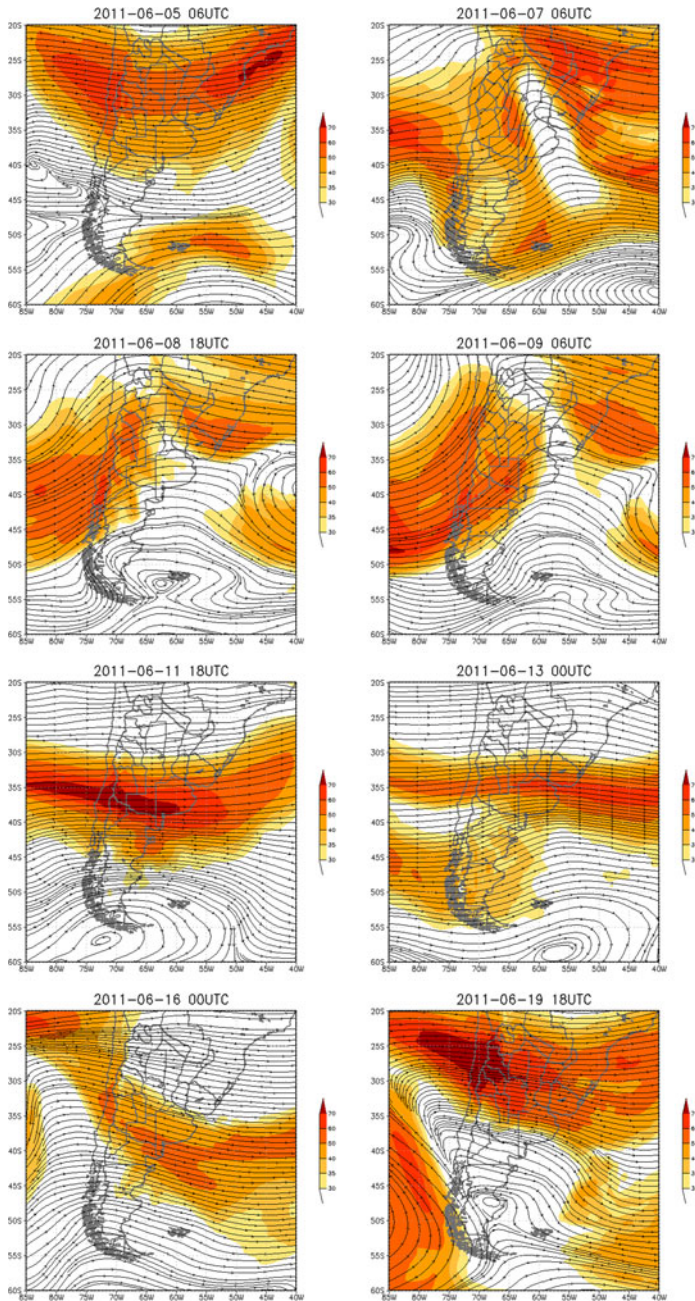


Fig. 8 Snapshots of the WRF-ARW meteorological forecast during the simulated period. The graphics show wind velocity in ms^{-1} (shaded) and streamlines at 250 hPa elevation during: **a** 05 Jun at 06 UTC, **b** 07 Jun at 06 UTC, **c** 08 Jun at 18 UTC, **d** 09 Jun at 06 UTC, **e** 11 Jun at 18 UTC, **f** 13 Jun at 00 UTC, **g** 16 Jun at 00 UTC and, **h** 19 Jun at 18 UTC

meteorological fields (here furnished off-line by the successive 72 h WRF/ARW forecasts) and volcanological inputs (source term and grain-size) to produce time-dependent 2D and 3D variables like airborne ash concentration, ash cloud column load and ground deposit thickness among others.

The FALL3D computational domain considered to model the Cordón Caulle eruption spans from 75°W to 45°W in longitude and from 50°S to 20°S in latitude, with spatial resolutions of 0.25° in the horizontal (this resolution is consistent with that of the meteorological driver) and 1 km in the vertical. We performed 72 h runs from 4 June 2011 at 18:45 UTC to 20 June 2011 at 00:00 UTC using the following volcanological inputs:

- Eruption column height. Daily averaged values were derived from in situ observations reported by SERNAGEOMIN and G. Villarosa, also from Buenos Aires VAAC and GOES-12 and AQUA satellite imagery. The cloud-top IR image, a technique that consists in enhancing the highest reflectance from IR images and nearby soundings (Kidder and VonderHaar 1995), allowed estimating the height of the eruption column when in situ observations were not available. The results are reported in Table 3. Moreover, the high temporal frequency of the GOES-12 products (~ 15 min) permitted to track the dispersion of the ash cloud.
- Total grain-size distribution (TGSD). A preliminary particle TGSD for the simulations was obtained during the first day of the eruption, following the field campaign. Ash samples were collected at Puerto Madryn (42°47'S, 65°01'W, 650 km ESE from Cordón Caulle) on 5 June and at “Planta Las Lajas” (43°37'S, 66°22'W, 600 km SE from Cordón Caulle) on the 7 June (Iglesias et al. 2011). The discretization of the TGSD assumes 10 bins ranging from -1Φ (2 mm) to 8Φ (4 μm) and assumed a standard linear dependency of particle density with diameter (values of 1,000 and 2,200 kg/m^3 were considered for the two end members). Clearly, this granulometry is incomplete and fine-skewed, so that our results cannot be expected to be accurate in the

Table 3 Daily average column height (km a.s.l.) used in the simulations for the 04–20 June 2011 period

Day—time (UTC)	Height (km)
04—18:45	10
05—00:00	10
06—00:00	10
07—00:00	6.5
08—00:00	7
09—00:00	8.5
10—00:00	8
11—00:00	6.5
12—00:00	7
13—00:00	8
14—00:00	7.5
15—00:00	8
16—00:00	7
17—00:00	5.5
18—00:00	5
19—00:00	4
20—00:00	4

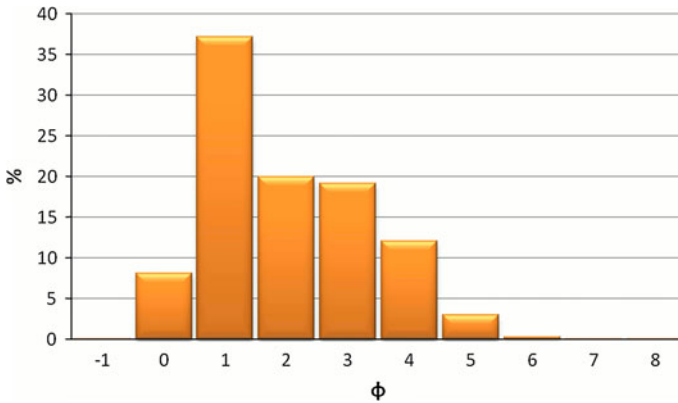


Fig. 9 Total grain-size distribution (TGSD) used in the simulations. The discretization of the TGSD assumes 10 bins ranging from -1Φ (2 mm) to 8Φ (4 μm). See text for details

proximal. Particle sphericity was set to a constant standard value of 0.9. The resulting histogram is shown in Fig. 9.

- Mass eruption rate (MER) and vertical distribution of mass in the column. In order to characterise the source term, we used the 1-D radially averaged buoyant plume theory (BPT) (Bursik 2001; Carazzo et al. 2008) to derive the MER and vertical distribution of mass given the height of the column (Table 3) and the conditions at the vent. For vent conditions, we assumed an exit velocity of 200 m/s and a mixture temperature of 980 °C. According to the BPT and considering the daily averaged column heights and vent conditions, the total mass erupted during the period between 4 and 19 June is of 2.4×10^{12} kg (averaged MER 1.7×10^6 kg/s). For comparison, an estimation of the erupted mass using the fit proposed by Mastin et al. (2009) gives 0.7×10^{12} kg (averaged MER 0.5×10^6 kg/s), a value about three times lower. Such a difference is within the typical range of uncertainty in the estimation of the MER for subplinian eruptions.

The model was set up to run with the Ganser, (1993) terminal velocity model and the CMAQ option (Byun and Ching 1999) to compute horizontal diffusion. The effects of ash aggregation were not considered. Finally, it is worth to mention that numerical weather prediction error grows as lapse time increases and, consequently, the use of recent forecasting cycles improves the accuracy of a forecast. In this study, and for the whole simulated period, we performed a “restart” of the FALL3D model every 72 h in correspondence with the WRF/ARW 72 h forecasting cycles. The configuration of the FALL3D model with the restart option implies the initialization of each FALL3D run with the previous airborne ash concentration and deposit as well as with the current meteorological fields.

6 Results and validation

6.1 Comparison with satellite retrievals

Here, we perform a qualitative comparison between our results and the NOAA-AVHRR satellite ash detection retrievals obtained by the high resolution picture transmission

(HRPT) division of the SMN. The SMN used the split window (SW) technique (Prata 1989) based on the brightness temperature difference between 11 and 12 μm spectral bands, where negative values indicate probable ash signal. Prata (1989) developed this methodology based on the larger emissivity of volcanic ash at the longer wavelength. The threshold values applied here were negative, using the colour enhancement technique ranging from red to yellow.

Figure 10 compares SW satellite retrievals with the model column mass (in ton/km^2), resulting from integrating the mass of the ash cloud along the atmospheric vertical levels. In general, it is expected that comparisons between forecasted mass column and retrievals differ at the outer limits of the ash cloud. Apart from lack of modelling accuracy, differences can also arise because satellite images detected only the top of the cloud rather than the whole column of ash and because of inherent limitations of the retrieval technique. In addition, this technique has some limitations (Ellrod et al. 2003) caused by the height of the eruption cloud, the mass per unit area of fine ash within the cloud, and the size of the ash particles (smaller particles have a stronger signal). Nevertheless, this method has a higher effectiveness for large eruptions (Rose and Mayberry 2000).

On 6 June, the plume dispersed following the trace of a trough and later directed northwards to reach the north of Argentina, Paraguay and the south of Brazil. During 7 June, our results show a lag of few hours with respect to the satellite observations, likely due to an underestimation of the intensity of the trough by the WRF/ARW meteorological driver. On 8 June, the wind turned to the west and the forecasted column mass presents a high correlation with the SW ash signal, including some dilute residual clouds observed by the satellite over Uruguay, Brazil and Paraguay after the passage of 7 June trough. Later, during the night, the trough became more intense, and the wind direction turned SW driving the ash dispersion throughout the trough-ridge structure.

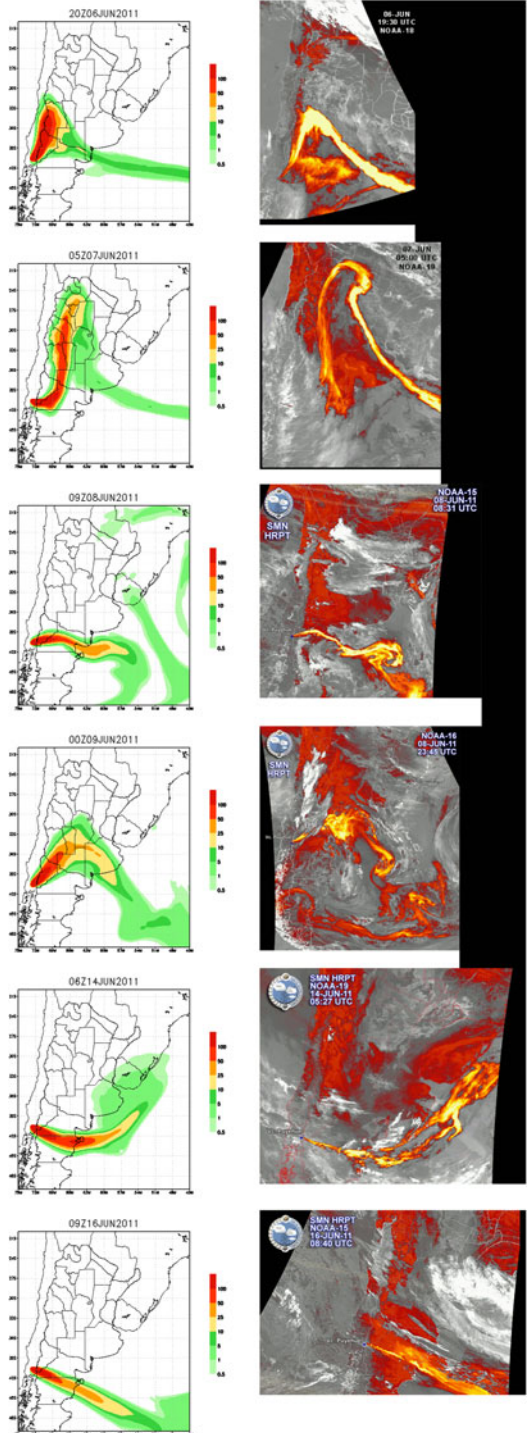
During 9 June, the ash cloud reached the city of Buenos Aires, where persisted until the 10 June after leaving a thin layer of ash. During the early hours of the 12 June, the volcanic plume dispersed W–SW affecting the north of Patagonia. Later at midday, a trough carried the plume again towards NE, reaching the central east portion of Argentina, Uruguay and the south of Brazil on the late hours of the 13 June (not shown). The comparison between the FALL3D forecasts and the satellite imagery shows a significant correlation across the ash cloud track. While the trough was travelling east, a postfrontal ridge was moving behind, and during the 14 June, the cloud followed the ridge structure to the NE. This feature was accurately forecasted by the model, which showed a high resemblance with the SW satellite signal.

On 16 June, the plume height was around 4 km, and early in the morning, the frontal flank of a ridge from the west diverted the western part of the plume again to S–SE, with strong N–NW winds. The forecast correlated well with the satellite images all during the day, albeit the ash signal was weak because of the low column height. Afterwards and until the end of the simulation, the plume was directed S–SE affecting the southern part of the Patagonia and Chile.

6.2 Comparison with measured ground deposit

Figure 11a shows the isopachs derived from measurements taken during 60 days after the beginning of the eruption, although we found no substantial difference when comparing with the first 30 days (not shown). This is partly due to the fact that we consider the accumulated deposits without taking into account the thickness variations produced by

Fig. 10 Composite showing the comparison between FALL3d column mass forecasts (ton km^{-2}), and split windows algorithm images. Results for **a** 6 June at 20 UTC, **b** 7 June at 05 UTC, **c** 8 June at 09 UTC, **d** 9 June at 0 UTC, **e** 14 June at 06 UTC, **f** 16 June at 09 UTC



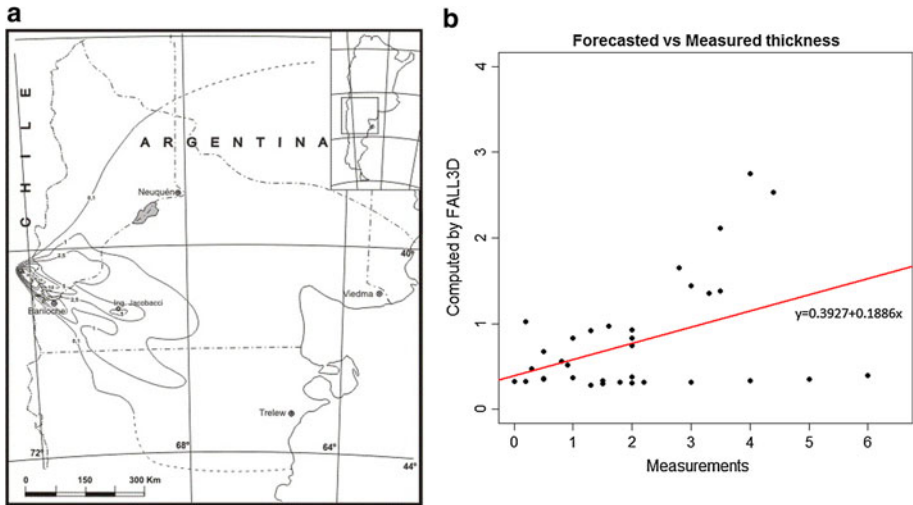


Fig. 11 **a** Measured ground deposit isopachs (in kg/m^2) for the period beginning on 4 June until 30 June. **b** Observed versus computed deposit thickness (cm). The solid line indicates a best fit

remobilization. It should be noted also that the sampling might be influenced by the difficulties to reach isolated regions. At some locations, up to 9 measurements were taken at different days, and in many cases, the thickness was obtained after a considerable amount of water was evaporated from the sample. The scatter plot (Fig. 11b) shows the comparison between the measured and the FALL3D computed deposit thickness at 37 sparsely distributed locations, all over two regions to the NE and to the SE of the vent. We also remark that differences can arise because the model calculates deposit load rather than thickness, so that a mean deposit density (not always measured) has to be assumed for the conversion.

6.3 Forecasting impacts on civil aviation

The FALL3D model can furnish values of airborne concentration at relevant flight levels. This variable is of interest for air traffic management purposes and can be used to design safe alternate routes. As an example, results of the forecast at flight level FL050 are shown in Fig. 12. From 4 to 6 June, the airspace forecasted to be contaminated was constrained within a latitude band between 38°S and 47°S . However, after the 6 June midday and until the 11 June at night, the volcanic plume twisted, and critical concentration values were forecasted within a wide area east of the Andes range (Fig. 12a). The results of the simulation suggest that the cancellation of multiple flights in several Argentinean airports during this period was justified. Another trough on 12 June deviated the ash plume north eastwards affecting the airspace up to the South of Brazil, and according to the model, critical values were achieved until the 14 June (Fig. 12c–e). On 17 June, a north eastwards moving trough advected the ash cloud down to 35°S and an intense ridge transported ash to the south of Patagonia following strong N–NW winds. This was the first time that the plume went south of latitude 48°S . From the 18 June, at midday and until the end of the simulated period, the model predicted contaminated areas south of 39°S and critical values in Southern Chile (Fig. 12f).

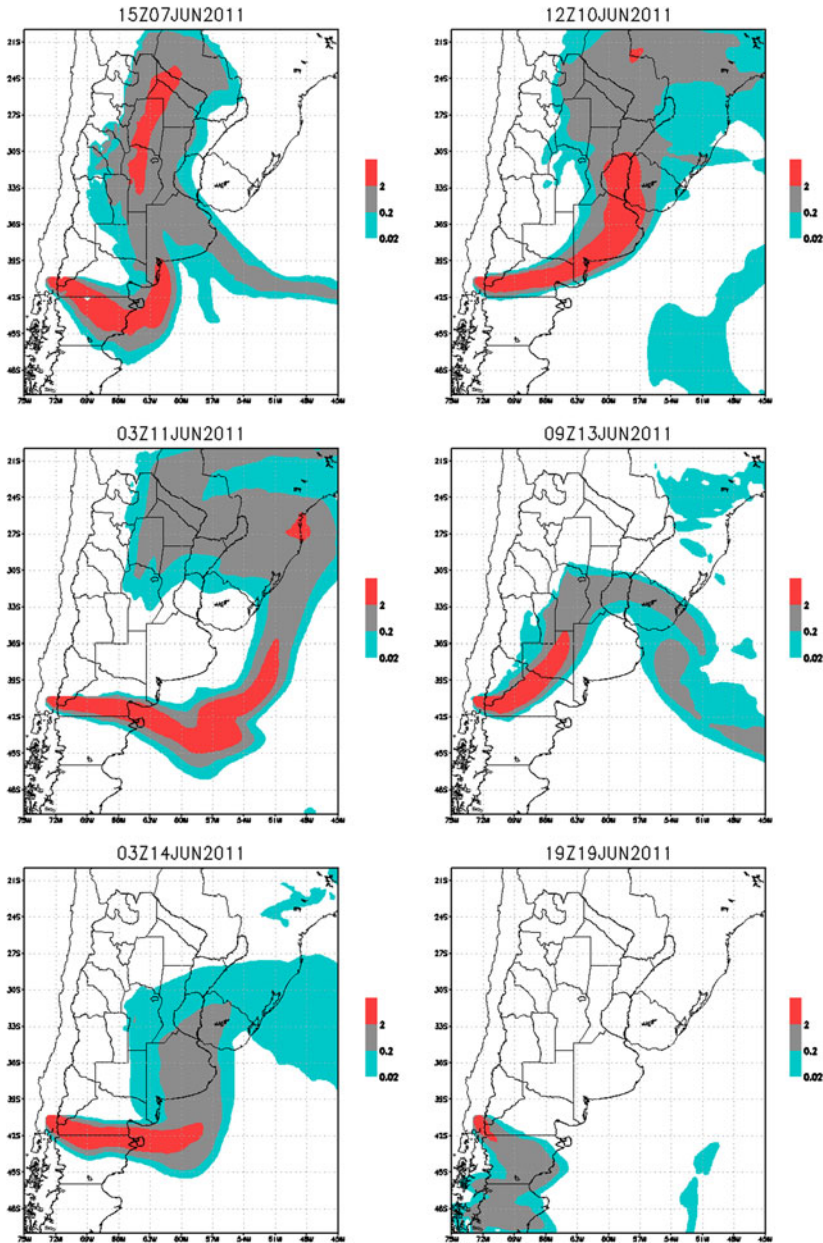
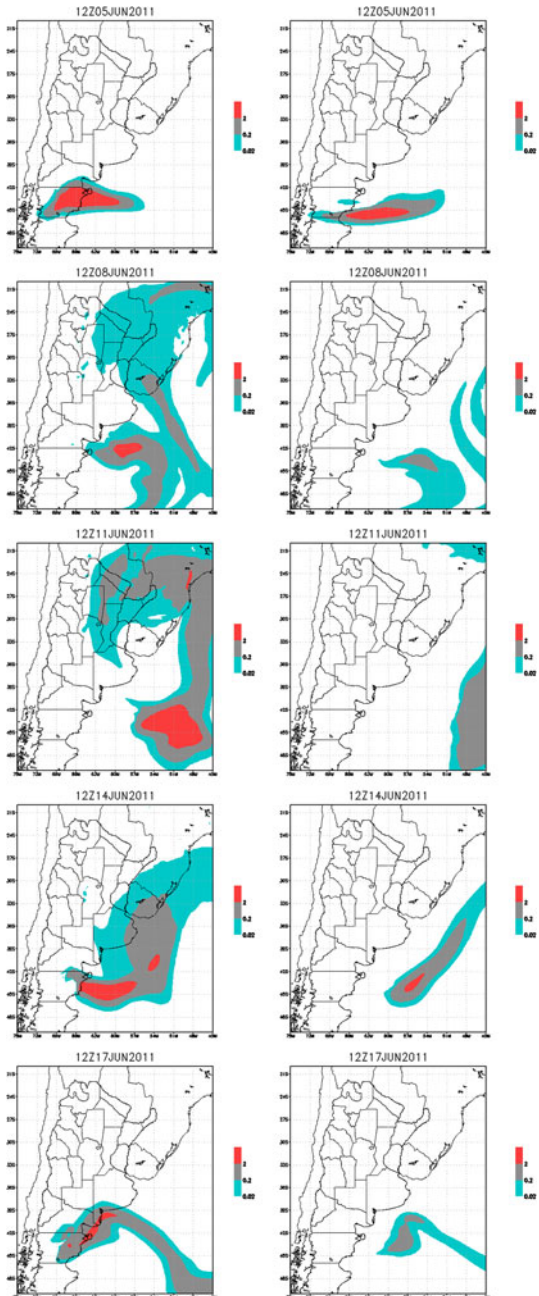


Fig. 12 Forecast of airborne ash concentration at FL050 (5,000 feet of nominal pressure, 1,500 m circa). Concentration contours of 2, 0.2 and 0.02 mg/m³ indicate the zones of high, medium and low contamination according to the UK Civil Aviation Authority and EUROCONTROL guidelines. Results for: **a** 07 Jun at 15 UTC, **b** 10 Jun at 12 UTC, **c** 13 Jun at 09 UTC, **d** 11 Jun at 03 UTC, **e** 14 Jun at 03 UTC and, **f** 19 Jun at 19 UTC

7 Summary and discussion

This paper documents the modelling of the 2011 Cordón Caulle eruption using the WRF/ARW-FALL3D forecasting system and the validation of the results using satellite imagery and in situ ground deposit measurements. A comprehensive synoptic analysis of the

Fig. 13 Differences between forecasts with and without restart option. Contours indicate values (i.e. differences) of 2, 0.2 and 0.02 mg/m^3 at FL050 (left column) and FL250 (right column). Note the large extent of the contaminated areas, especially at FL050, which are not predicted when restart is not considered. Results for **a** 05 Jun at 00UTC, **b** 08 Jun at 00UTC, **c** 11 Jun at 00UTC, **d** 14 Jun at 00UTC and, **e** 17 Jun at 00UTC



meteorological situation during the selected period obtained from the WRF–ARW forecasts was furnished to the FALL3D dispersal model together with inputs inferred from ash samples taken at distal locations.

For evaluation purposes, we performed a qualitative comparison between model forecasts and satellite imagery, obtaining a good correlation regardless of the remote sensing and modelling limitations. These may include, among others, the presence of meteorological clouds and the occurrence of aggregation processes not contemplated by the simulations. On the other hand, results for ash concentration at relevant flight levels during the first weeks of the episode helps to improve the operational forecasting strategy. Typically, operational systems forecast few days ahead only. For example, the SHN–SMN strategy analysed here makes use of daily 72 h WRF/ARW forecasts, and obviously, this constrains the period of the dispersion forecast. On the other hand, and more importantly, volcanological inputs required by dispersal models can vary frequently as a result of the (uncertain) transient eruptive behaviour. As a consequence, forecasting during long-lasting events typically involves a series of short-term forecasts. In this context, a critical issue is to dispose of a restart mode for the dispersion model that accounts for the existence of airborne ash when a run starts. The magnitude of the error when neglecting the restart depends on several factors such as wind direction and intensity, column height, extent of the computational domain, etc., but in general, the differences between considering and not considering the restart option can be very large. This is illustrated in Fig. 13, which shows the effect of subtracting the no restart to the restart forecast (i.e., it quantifies the error committed in the no restart case). It can be observed how large areas with positive values (over the critical 2 mg/m^3) disappear if the forecast neglects the restart, resulting in a model underestimation of the critical areas.

This paper has shown the usefulness of the combined WRF/ARW-FALL3D forecasting system for tracking ash cloud movement, evaluating the concentration of ash at different flight levels, and simulating the deposition of ash on the ground. This provides an invaluable tool, especially for countries that, due to large sizes, have difficulties in monitoring volcanoes in remote areas.

Acknowledgments This work has been partially funded by Spanish Research Project ATMOST (CGL2009-10244), the CYTED thematic network CENIZA (410RT0392), and CONICET. AF is grateful to the Ramón y Cajal scientific programme. Simulations have been done at the facilities of the Barcelona Supercomputing Center (BSC-CNS) using the *MareNostrum* supercomputer. The WRF/ARW-FALL3D modelling system was implemented in a cluster installed at the SMN with funds from the Argentinean project PIDDEF 41/10 which also support partly this research. We thank Diana M. Rodríguez and Silvana K. Bolzi from the HRPT Division (SMN), Claudio Iglesias (Piedra Grande S.A.), Graciela Massaferro (Centro Nacional Patagónico CENPAT–CONICET), Nilda Menegatti (Univ. de la Patagonia San Juan Bosco), Walter Baez (INENCO-CONICET), Rodolfo Ugarte (Yacimientos Petrolíferos Fiscales, YPF), the Nahuel Huapi National Park rangers and Gendarmería from Villa La Angostura that made the Argentinean ash network work, providing the samples for grain-size analyses Dr. Eduardo Gómez (Instituto Argentino de Oceanografía, IADO-CONICET) for grain-size data, and Adrián Moyano for his advice on Mapuche language. Finally, we also thank Ma. Noel Serra, Valeria Outes, Débora Beigt and Ma. Andrea Dzendoletas (INIBIOMA, Universidad Nacional del Comahue). We thank to Comisión de Actividades Espaciales (CONAE) for the COSMO –SKYmed images. The comments from two anonymous referees improved the early version of this manuscript.

References

- Bentley MJ (1997) Relative and radiocarbon chronology of two former glaciers in the Chilean Lake District. *J Quat Sci* 12:25–33

- Bursik M (2001) Effect of wind on the rise height of volcanic plumes. *Geophys Res Lett* 18:3621–3624
- Byun D, Ching J (1999) Science algorithms of the EPA Models-3 community multiscale air quality modeling system. EPA/600/R-99/030. US Environmental Protection Agency, Office of Research and Development, Washington, DC
- Cahill T, Isacks B (1992) Seismicity and shape of the subducted Nazca plate. *J Geophys Res* 97:17503–17529
- Campos A, Moreno H, Muñoz J, Antinao J, Clayton J, Martin M (1998) Área de Futrono-Lago Ranco, Región de los Lagos, Servicio Nacional de Geología y Minería, Mapas Geológicos No.8, 1 mapa escala 1:100.000. Santiago de Chile
- Carazzo G, Kaminski E, Tait S (2008) On the dynamics of volcanic columns: a comparison of field data with new model of negatively buoyant jets. *J Volcanol Geotherm Res* 178:94–103
- Cembrano J, Hervé F, Lavenu A (1996) The Liquiñe–Ofqui fault zone: a long-lived intra-arc fault system in southern Chile. *Tectonophysics* 259:55–66
- Chapron E, Ariztegui D, Mulsoo S, Villarosa G, Pino M, Outes V, Juvignié E, Crivelli E (2006) Impact of 1960 major subduction earthquake in Northern Patagonia (Chile, Argentina). *Quat Int* 158:58–71
- Costa A, Macedonio G, Folch A (2006) A three-dimensional Eulerian model for transport and deposition of volcanic ashes. *Earth Planet Sci Lett* 241:634–647
- DeMets C, Gordon R, Argus D, Stein S (1994) Effect of recent revisions to the geomagnetic reversal time scale on estimates of current plate motions. *Geophys Res Lett* 21:2191–2194
- Denton GH, Heusser CJ, Lowell TV, Moreno PI, Andersen BG, Heusser LE, Schluchter C, Marchant DR (1999) Interhemispheric linkage of paleoclimate during the last glaciation. *Geogr Ann* 81:107–153
- Dudhia J (1989) Numerical study of convection observed during the winter monsoon experiment using a meso scale two-dimensional model. *J Atmos Sci* 46:3077–3107
- Ellrod GP, Connell BH, Hillger DW (2003) Improved detection of airborne volcanic ash using multi-spectral infrared satellite data. *J Geophys Res* 108:4356
- Folch A, Jorba O, Viramonte JG (2008) Volcanic ash forecast—application to the May 2008 Chaitén eruption. *Natl Hazards Earth Syst Sci* 8:927–940
- Folch A, Costa A, Macedonio G (2009) FALL3D: a computational model for volcanic ash transport and deposition. *Comput Geosci* 35(6):1334–1342
- Folch A, Osoreo MS, Pujol G, Collini E, Suaya M (2011) Evaluation of the FALL3D model using WRF–ARW fields for the 2008 Chaitén eruption. European Geosciences Union General Assembly 2011 (EGU 2011)
- Ganser G (1993) A rational approach to drag prediction of spherical and non spherical particles. *Powder Technol* 77:143–152
- Gerlach D, Frey F, Moreno H, López L (1988) Recent volcanism in the Puyehue–Cordón Caulle region, Southern Andes, Chile (40.5°S): petrogenesis of evolved lavas. *J Petrol* 29:333–382
- Hildreth W, Moorbath S (1988) Crustal contributions to arc magmatism in the Andes of Central Chile. *Contrib Mineral Petrol* 98:455–489
- Iglesias C, Lobos M, Lago J (2011) Lluvia de cenizas volcánicas en el área valle inferior del río Chubut. Internal Report from Piedra Grande SA
- Kanamori H, Cipar JJ (1974) Focal process of the great Chilean earthquake, May 22, 1960. *Phys Earth Planet Inter* 9:128–136
- Kidder SQ, VonderHaar TH (1995) Satellite meteorology: an introduction. Academic Press, NY
- Lara LE, Moreno H (2006) Geología del Complejo Volcánico Puyehue–Cordón Caulle, X Región de Los Lagos, Servicio Nacional de Geología y Minería, Carta Geológica de Chile, Serie Geología Básica, 1 mapa escala 1:50.000
- Lara LE, Rodríguez C, Moreno H, Pérez de Arce C (2001) Geocronología K–Ar y geoquímica del volcanismo plioceno superior–pleistoceno de los Andes del Sur (39°–42°S). *Rev Geol Chile* 28:67–90
- Lara LE, Mathews S, Pérez C, Moreno H (2003) Evolución morfoestructural del Complejo Volcánico Cordón Caulle (40°S): evidencias geocronológicas 40Ar–39Ar. In Proceedings of the 10th Congreso Geológico Chileno, Concepción, Electronic Files
- Lara LE, Naranjo JA, Moreno H (2004) Rhyodacitic fissure eruption in Southern Andes (Cordón Caulle; 40.5°S) after the 1960 (Mw: 9.5) Chilean earthquake: a structural interpretation. *J Volcanol Geotherm Res* 138:127–138
- Lara LE, Lavenu A, Cembrano J, Rodríguez C (2006a) Structural controls of volcanism in transversal chains: resheared faults and neotectonics in Cordón Caulle–Puyehue area (40.5°S), Southern Andes. *J Volcanol Geotherm Res* 158:70–86
- Lara LE, Moreno H, Naranjo JA, Mathews S, Pérez de Arce C (2006b) Magmatic evolution of the Puyehue–Cordón Caulle volcanic complex (40°S), Southern Andean Volcanic Zone: from shield to unusual rhyolitic fissure volcanism. *J Volcanol Geotherm Res* 157:343–366

- Lavenu A, Cembrano J (1999) Compressional and transpressional stress pattern for Pliocene and Quaternary brittle deformation in fore arc and intra-arc zones (Andes of Central and Southern Chile). *J Struct Geol* 21:1669–1691
- Le Maitre RW, Streckeisen A, Zanettin B, Le Bas MJ, Bonin B, Bateman P, Bellieni G, Dudek A, Efremova S, Keller J, Lamere J, Sabine PA, Schmid R, Sorensen H, Woolley AR (2002) Igneous rocks: a classification and glossary of terms, recommendations of the international union of geological sciences, subcommission of the systematics of igneous rocks. Cambridge University Press, ISBN 0-521-66215-X
- Lowell TV, Heusser CJ, Andersen BG, Moreno PI, Hauser A, Heusser LE, Schluchter C, Marchant DR, Denton G (1995) Interhemispheric correlation of late Pleistocene glacial events. *Science* 269:1541–1549
- Mastin LG, Guffanti M, Servranckx R, Webley P, Barsotti S, Dean K, Durant A, Ewert JW, Neri A, Rose WI, Schneider D, Siebert L, Stunder B, Swanson G, Tupper A, Volentik A, Waythomas CF (2009) A multidisciplinary effort to assign realistic source parameters to models of volcanic ash-cloud transport and dispersion during eruptions. *J Volcanol Geotherm Res* 186:10–21
- Michalakes J, Dudhia J, Gill D, Henderson T, Klemp J, Skamarock W, Wang W (2005) The weather research and forecasting model: software architecture and performance. In: Zwiefhofer W, Mozdzyński G (eds) Proceedings of the eleventh ECMWF workshop on the use of high performance computing in meteorology, World Scientific
- Mlawer E, Taubman S, Brown P, Iacono M, Clough S (1997) Radiative transfer for inhomogeneous atmosphere: RRTM, a validated correlated-k model for the longwave. *J Geophys Res* 102:16663–16682
- Moreno H (1977) Geología del área volcánica Puyehue-Carrán en los Andes del sur de Chile, (unpublished thesis). Universidad de Chile, Santiago
- Moreno H, Petit-Breuilh ME (1999) El volcán fisural Cordón Caulle, Andes del Sur (40.5°S): geología general y comportamiento eruptivo histórico. 14th Congreso Geológico Argentino, Actas (vol 2) Salta, Argentina, pp 258–260
- Osores MS, Pujol G, Collini E, Folch A (2011) Análisis de la dispersión de ceniza volcánica en la atmósfera modelada por el FALL3D para la erupción del volcán Hudson en 1991. Publicación en las actas de la Conferencia Geográfica Regional 2011 (UGI), Santiago de Chile
- Prata AJ (1989) Observations of volcanic ash clouds in the 10–12 μm window using AVHRR/2 data. *Int J Remote Sens* 10(4–5):751–761
- Rose WI, Mayberry GC (2000) Use of GOES thermal infrared imagery for eruption scale measurements, Soufriere Hills, Montserrat. *Geophys Res Lett* 27:3097–3100
- Singer B, Jicha BR, Harper MA, Naranjo JA, Lara LE, Moreno-Roa H (2008) Eruptive history, geochronology, and magmatic evolution of the Puyehue-Cordón Caulle volcanic complex, Chile. *GSA Bull* 120(5/6):599–618. doi:10.1130/B26276.1; 12 figures; 3 tables; Data Repository item 2008026
- Tamaki K (2000) Nuvel 1-A calculation results. Ocean Research Institute. University of Tokio. http://ofgs.ori.u-tokyo.ac.jp/~okinno/rate_calc_new.cgi
- Tassara A, Yáñez G (2003) Relación entre el espesor elástico de la litósfera y la segmentación tectónica del margen andino (15–47°S). *Rev Geol Chile* 30:159–186
- Villarosa G (2008) Tefrocronología Postglacial de la región de Nahuel Huapi, Patagonia, Argentina. PhD Thesis, Unpublished
- Villarosa G, Outes V (2008) Rutina de toma de muestras de tefra: Procedimientos para coleccionar muestras de ceniza. INIBIOMA (CONICET-Universidad Nacional del Comahue) Booklet, 6 pp
- Villarosa G, Outes V, Hajduk A, Montero EC, Selles D, Fernandez M, Crivelli E (2006) Explosive volcanism during the Holocene in the Upper Limay River Basin: the effects of ashfalls on human societies, Northern Patagonia, Argentina. *Quat Int* 158:44–57